



A promising N-doped carbon-metal oxide hybrid electrocatalyst derived from crustacean's shells: Oxygen reduction and oxygen evolution



Gumaa A. El-Nagar^{a,b,*}, Mohamed A. Hassan^c, Abdulmonem Fetyan^b, Manoj Krishna Kayarkatte^b, Iver Lauermann^d, Christina Roth^{b,*}

^a Chemistry Department, Faculty of Science, Cairo University, Cairo 12613, Egypt

^b Institute of Chemistry and Biochemistry, FU Berlin, Takustr. 3, D-14195 Berlin, Germany

^c Nanotechnology and Advanced Materials Central Lab, Agriculture Research Center, Giza, Egypt

^d Helmholtz-Zentrum Berlin für Materialien und Energie, Hahn-Meitner-Platz 1, 14109 Berlin, Germany

ARTICLE INFO

Article history:

Received 16 March 2017

Received in revised form 5 May 2017

Accepted 9 May 2017

Available online 10 May 2017

Keywords:

Chitosan

N-doped

ORR

OER

Fuel cells

Impurities

ABSTRACT

The development of efficient and durable Pt-free catalysts for the oxygen reduction reaction (ORR) is extremely important to realize the world-wide commercialization of the clean energy technologies obstructed by the high cost and scarcity of the Pt-based catalysts. As a potential alternative to such catalysts, this investigation addresses the facile synthesis of an efficient, durable and highly poison-tolerant metal-free N-doped carbon-Nd₂O₃ hybrid bifunctional electro-catalyst for ORR and water splitting compared to commercial Pt/C catalyst. Chitosan obtained from crustacean's shells assists to yield a nitrogen-doped graphitic structure with superior activity and durability for ORR. Nd₂O₃/N-C shows a high tolerance towards crossover of various anodic fuels concurrent with high poisoning tolerance against various hydrocarbon impurities *in-situ* generated during fuel cell operation. H₂-air single cell tests using Nd₂O₃/N-C as cathode catalyst delivered outstanding power density (~287 mW cm⁻²) and current density (~572 mA cm⁻²) at 0.6 V. The superior electro-catalytic activity and durability of the as-prepared catalysts mainly originates from the synergistic effects between Nd₂O₃_{nano} particles and the nitrogen-doped graphitic structure. The facile synthesis method and the high performance together with low-cost of our suggested Pt-free catalyst make it as a promising alternative for the commercial Pt/C.

© 2017 Elsevier B.V. All rights reserved.

1. Introduction

Renewable energy resources such as supercapacitors, metal-air batteries, lithium-ion batteries and unitized regenerative fuel cells have been recognized as promising alternative energy conversion and storage systems with high efficiency, environmental benignity and great potential to lessen the ever-increasing pressure from society's energy deficiency [1–10]. Nevertheless, their widespread commercialization and application in real-world devices have been dramatically hindered by the sluggish kinetics of the oxygen reduction (ORR) and oxygen evolution (OER) reactions which are the essential electrode processes that govern the performance of metal-air batteries and unitized regenerative fuel cells

[1,3,11–15]. Regardless of the tremendous efforts, the development of low-priced bifunctional catalysts (ORR & OER) with high activity and durability remains a great challenge, i.e., the current bottleneck of unitized regenerative fuel cells is the sluggish ORR kinetics. Pt-based catalysts are recognized as the best known ORR catalysts, however, their high cost, scarcity and for practical applications comparatively low durability due to inevitable Pt dissolution/agglomeration, in addition to their poor tolerance against operation-inherent organic and/or inorganic contaminants hamper their widespread use and commercial success [10,16–19]. Consequently, a potential budget alternative to such expensive catalysts with high durability and performance based on non-precious metal or metal oxides has been enthusiastically pursued [1,3,10,12,16,18]. On the other hand, water splitting (the reverse reaction of ORR and OER) plays a vital role in energy conversion and storage technologies, such as fuel cells and solar fuel synthesis [1,3,20,21]. Iridium and ruthenium oxide-based catalysts have an extraordinary OER activity, while at the same time they exhibit

* Corresponding authors.

E-mail addresses: elnagar087@yahoo.com (G.A. El-Nagar), christina.roth@fu-berlin.de (C. Roth).

only low ORR activity [1,3,22–24] (N.B., efficient catalysts for the ORR generally tend to be poor for the OER and vice versa [1,25,26]). Thus the development of efficient bifunctional catalysts for ORR and OER is highly challenging but necessary, particularly for un-tized regenerative fuel cells, a promising energy storage system that works as a fuel cell and in reverse as a water electrolyzer producing H₂ and O₂ to feed the fuel cell.

Intensive efforts have been dedicated to develop highly active and budget bifunctional catalysts with at least an activity comparable to that of the commercial Pt catalyst, but with a better stability and higher tolerance against various fuels crossover and impurities, such as transition-metal oxides [10,16,27], transition metal nitrides/carbides [28,29], and carbon-based nanomaterials [30–33]. Conspicuously, carbon-based materials are considered as promising catalysts based on their low cost and durability. Among these carbon materials, nitrogen-doped carbon (NC) based catalysts, including nanotubes, graphite materials and graphene, have attracted the most attention as an excellent alternative catalyst for Pt in order to enhance commercialization prospect of renewable energy technologies [34–37]. Generally, heteroatom (e.g., nitrogen) doping of carbon can enhance its electrical properties, supply potentially active sites for oxygen reduction (via creating positively charged sites) and favor and strengthen the initial chemical adsorption of oxygen on the catalyst surface [35,36,38]. However, the low content of nitrogen ($\leq 5\%$) and scarcity of nitrogen active sites always lead to unsatisfying stability and activity of nitrogen-doped catalysts for ORR [36]. The development of NG materials with more nitrogen active sites and relatively higher nitrogen content is therefore highly desirable. There are two different approaches for N-doped carbon-based materials synthesis; post-doping, wherein chemical pretreatment in HCN, NH₃ or HNO₃ is generally used to introduce N atoms [39–43]. This might result in a poor reproducibility, homogeneity and crystal structure compared to the approach of in-situ direct-doping [42,43]. However, these methods have noticeable disadvantages including low efficiency, residual metallic impurities, and requirement of multiple organic precursors. Thus, the development of a highly efficient, ecofriendly and green synthesis route for Pt-free N-doped-based materials with superior activity toward ORR is highly desirable as is knowledge of the nature of the catalytic sites.

About 6–8 million tonnes of waste crustacean shells (e.g., crab, shrimp and lobster) containing 20–40% protein, 20–50% calcium carbonates and 15–40% chitin are produced world-wide. However, the potential value of such shells is being ignored in the chemical industry [44,45]. Chitin is a linear polymer containing nitrogen and the second most abundant natural biopolymer on earth after cellulose [44,46]. At this time, it and its water-soluble derivative, chitosan, are used in only a few niche areas of industrial chemistry, such as cosmetics, textiles, water treatment and biomedicine. Moreover, neodymium and its oxides have attracted a great interest in recent years due to their potential use in photo-catalysis [47], and other applications [48–50]. With neodymium's low electronegativity and high binding strength of Nd–O, neodymium is considered to be an excellent binder to oxygen [51]. Despite belonging to the group of rare earth elements, neodymium is a common element and widely distributed in the Earth's crust.

In this regards, this study introduces the synthesis of a highly active nitrogen-doped carbon (N–C) by the thermal decomposition of chitosan matrix, for the first time. Chitosan is a natural biopolymer which is obtained by de-N-acetylation of chitin [5,8,52]. Moreover, neodymium oxide nanostructured (nano-Nd₂O₃) encapsulated in N-doped graphitic structure (Nd₂O₃/N–C) is prepared by annealing of chitosan-Nd(OH)₃ microspheres (N.b., Nd(OH)₃ is in-situ formed inside the chitosan matrix) as well. Additionally, this investigation reports the effect of various hydrocarbon impurities in-situ generated during fuel cell operation from the degradation

of various fuel cell components on the durability and the activity of the as-prepared catalyst compared to the commercial Pt/C catalyst. In addition, the effect of various anodic fuels crossover, such as formic acid, ethanol, methanol and ethylene glycol, on the stability and performance of the as-prepared catalyst is studied.

2. Methods

2.1. Materials synthesis

2.1.1. The synthesis of nitrogen-doped carbon (N–C) was carried out as follows: first, 1.0 g of chitosan was dissolved in 100 ml of 1% (v/v) acetic acid solution

The dissolution process was carried out at room temperature with stirring for 24 h. Next, the obtained bright yellow chitosan solution was drop-wise added into 0.5 M NaOH precipitation bath under magnetic stirring in order to form chitosan microspheres. The obtained chitosan microspheres were then filtered and washed intensively with distilled water, until a neutral pH was reached, followed by overnight drying at 70 °C. The dried chitosan microspheres (average diameter was 0.62 μm) were then heat treated at 700 °C for 3 h under nitrogen atmosphere to produce N-doped carbon (NC) via thermal decomposition of the chitosan matrix structure (N.b., chitosan structure decomposes above 300 °C, See scheme S1 [5,8,53]).

2.1.2. Nitrogen-doped carbon-neodymium oxide nanostructured hybrid (Nd₂O₃/N–C)

Synthesis was carried out as follows: First, chitosan-neodymium hydroxide microspheres are prepared, whereas 1.0 mg of neodymium (III) nitrate hexahydrate (Nd(NO₃)₃ · 6H₂O) was mixed with acidic chitosan solution with concentration of 1% (w/v) under vigorous stirring for at least 4 h to allow the chitosan matrix to adsorb the neodymium via its –NH₂ and –OH like functional groups and form some kind of chitosan-neodymium complex (See scheme S1). Next, the obtained chitosan-neodymium solution was dropped in 0.5 M NaOH precipitation bath to produce chitosan-neodymium hydroxide microspheres, in which neodymium oxide was in-situ formed inside the chitosan membrane during titration with NaOH. The obtained chitosan-neodymium hydroxide composite microspheres (nano-CS-Nd(OH)₃, average diameter was 0.64 μm) were kept under stirring for 2 h at room temperature and then filtered and washed with copious amounts of distilled water to remove the excess NaOH and neodymium from the microspheres surface. Afterwards, the obtained nano-CS-Nd(OH)₃ microspheres were dried at 70 °C for 24 h and then calcined at 700 °C for 3 h under flowing nitrogen to produce the nitrogen-doped carbon-neodymium oxide hybrid catalyst material (Nd₂O₃/N–C). On the other hand, the above described steps were used to synthesize nitrogen-doped neodymium oxide (N–Nd₂O₃) using heat treatment at 800 °C under air atmosphere in order to get rid of carbon. Furthermore, the pure neodymium oxide powder was prepared by the same process without using chitosan for comparsion.

2.2. Electrode preparation and electrochemical characterizations

The working electrode was prepared as follows: first, the as-prepared catalysts were finely ground to powder in an agate mortar and then 4 mg of the as-prepared catalyst was dispersed in 750 μl deionized water and 250 μl isopropanol solution containing 40 μl of Nafion aqueous solution. The above mixture was then ultrasonicated for 2 h to obtain a homogeneous catalyst ink. In order to prepare the working electrode for the electrochemical measurements, 5 μl of the freshly prepared ink was cast onto the mirror polished glassy carbon electrode followed by drying in air.

Electrochemical measurements were conducted with a Galvanostat/Potentiostat Reference 3000 (Gamry Instruments) at room temperature in a conventional three-electrode glass cell with a Pt spiral as a counter electrode, saturated calomel electrode (SCE with potential of 0.238 V) as a reference electrode and glassy carbon electrode loaded with different catalysts as a working electrode. 19 µg of the as-prepared catalysts were loaded atop glassy carbon electrode surface and glassy carbon rotating disk electrodes surface (3 mm in diameter). The scan rate was 5 mV/s for all electrochemical measurements.

2.3. Materials characterization

A scanning electron microscope (SEM, HITACHI UHR FE-SEM SU8030) and High resolution transmission electron microscope (HR-TEM, Tecnai G20, FEI, Netherland) coupled with an energy dispersive X-ray spectrometer (EDS), was used to evaluate the electrode morphology and composition. X-ray diffraction (XRD) was recorded in transmission geometry using a STOE STADI-Operated with Cu K α ($\lambda = 1.54 \text{ \AA}$) radiation and position sensitive detector used to identify the change in the morphology, the particle size and the crystallographic structure of the as prepared catalysts. X-ray photoelectron spectroscopy (XPS, CLAM4 electron analyzer from Thermo VG scientific), using a Mg K α X-ray source (1254 eV) was used to determine the samples chemical composition. For evaluation, a linear background was subtracted and peaks were fitted using Voigt functions with identical FWHM for each component of the same element [54]. Raman spectra were recorded on a RENISHAW inVia Raman microscope with an Ar laser source of 633 nm. The fitted peaks of the XPS and Raman spectra were attributed to the most probable assignment according to literature.

2.4. MEAs preparation and fuel cell testing

For the realistic fuel cell testing, the cathode (cathode loading $\sim 0.3 \text{ mg/cm}^2$) is made from N–C and Nd₂O₃/N–C nanosstructured material by using the standard airbrush method [55,56] which is sandwiched between the GDL (Sigracet28BC) and the Nafion 112-Ionpower membrane, while the anode (anode loading $\sim 0.1 \text{ mg/cm}^2$) is a painted GDL containing the commercial catalyst (HiSpec 3000, AlfaAesar) prepared using the standard airbrush method [55,56]. Fuel cell polarization curves were measured using a Scribner Series 850e test station with fully-humidified anode and cathode feed. The used single cells are made to harbour a 3.3 cm diameter round membrane-electrode-assembly. Experiments in H₂/O₂ setups were performed at 80 °C with fully humidified hydrogen (300 ml/min) into the anode side and fully humidified oxygen (300 ml/min) into the cathode side at 0.2 MPa. The membrane electrode assemblies (MEAs) were conditioned by holding the potential at 0.6 V overnight and gradually increasing the temperature to 80 °C until steady power output from the MEA was achieved. Polarization curves were generated by collecting the current at a given voltage after waiting 60–120 s for the system to stabilize by taking values linearly.

3. Results and discussion

3.1. Material characterization

The morphology and structure of the as-prepared catalysts before and after calcination at 700 °C for 3 h under nitrogen atmosphere were investigated by SEM-EDS, XRD and XPS. SEM micrographs show a substantial change in the morphologies of the as-prepared catalysts before and after calcination (Fig. 1 A–E). For instance, nano-chitosan (nano-CS, Image A) and nano-chitosan embedded with neodymium hydroxide (nano-CS-Nd(OH)₃, Image

D) have a spongy-like structure before heat treatment. They show agglomerations of ill-hollow tube like structure (assigned as N–C, Image B) and a nano-plate like structure (assigned as Nd₂O₃/N–C, image E) after calcination, respectively. On the other hand, pure neodymium hydroxide (Nd(OH)₃) has an agglomeration of irregular shape structure (Fig. S1 A) before annealing converting into island-like structured pure neodymium oxide (assigned as Nd₂O₃, Image C) with calcination. Additionally, TEM of Nd₂O₃/N–C revealed the hybrid formation of N–C and Nd₂O₃ (Image F and Fig. S1B) and its HR-TEM showed the crystalline spinel structure of Nd₂O₃ nanocrystals (Fig. S1C) consistent with its XRD pattern (C.F., Fig. S3). EDS analysis of nano-CS electrode exhibits a strong peak for nitrogen before and after annealing at 700 °C (N.b., chitosan matrix is decomposed at ca. 300 °C as revealed from TGA analysis, data not shown [5,8,53]) with homogeneous nitrogen atom distribution as revealed from its respective mapping (see Fig. S2).

This finding might suggest the formation of a nitrogen doped carbon after the decomposition of the chitosan structure. Moreover, the mapping EDS analysis of Nd₂O₃/N–C electrode displays a strong and well-distributed peak of nitrogen as well, besides oxygen and neodymium peaks, suggesting the formation of Nd₂O₃/N–C hybrid structures. Nd₂O₃/N–C has a greater amount of nitrogen compared to N–C electrode that might indicate the doping of both neodymium oxide and carbon after the destruction of chitosan at 700 °C. The crystallinity and structure of the as-prepared catalysts were further examined using XRD (data are presented in Fig. S3). The XRD pattern of nano-CS before calcination exhibited only one broad peak at $2\Theta \approx 20^\circ$ attributed to C (002) indicating the amorphous structure of chitosan, while N–C derived from thermal decomposition of chitosan showed a similar broad (002) peak centered at 23.7° and smaller broad (100) peak at 44° (average particle size $\sim 68 \text{ nm}$ as estimated using Scherrer's formula [5,57]). On the other hand, Nd₂O₃/N–C and pure Nd₂O₃ electrodes exhibited only the hexagonal crystalline Nd₂O₃ phase (JCPDS Card 65–6729). The calculated mean particle sizes using Scherrer's formula were 60 nm and 45 nm for the pure calcined Nd₂O₃ and Nd₂O₃/N–C electrodes, respectively. The smaller particle size of Nd₂O₃/N–C compared to that of pure Nd₂O₃ is attributed to the essential role of chitosan in the smaller particles formation yielding more homogeneously distributed catalytic sites [5,8].

Doped nitrogen heteroatoms in Pt-free catalysts exert an essential effect on the catalyst activity towards ORR, thus X-ray photoelectron spectroscopy (XPS) was applied to monitor the nature, amount and configuration of the nitrogen dopants in the as-prepared catalyst (Fig. 2). The fitted peaks are assigned to the most likely functional group according to literature. The high resolution XPS C1 s spectrum of the chitosan microspheres before calcination (assigned as nano-CS) can be deconvoluted into four peaks (Fig. 2A). The C1 s peak at $\sim 285 \text{ eV}$ was mainly attributed to C–C, C–H, but also to C–NH₂ chemical binding, given that amines are reported to induce small chemical shifts ($\sim 0.6 \text{ eV}$) [58–60]. The peak at $\sim 287 \text{ eV}$ was attributed to C–O and C=N, while the peak at $\sim 288.3 \text{ eV}$ was assigned to C=O and N–C–O chemical binding. The peak at $\sim 289 \text{ eV}$ attributed to O=C–O and O–C–O (N.B., C–O, O–C–O and O=C–O bonds can be assigned to alcoholic, ether and carboxylate groups) [60–63]. On the other hand, the XPS C1 s peak of the N-doped carbon (N–C), which is obtained by annealing the chitosan microspheres at 700 °C, shows an asymmetric peak shape with its main component at 285 eV was attributed only to carbon bound to carbon and hydrogen (i.e., indicating that the formed carbons are present in the sp² graphite structure, Fig. 2B) [1,64]. The other peaks at a higher binding energy were attributed to various C–O bonding configurations, C–O bonds and C=N bonds, C=O and C–N bonds, and O–C=O bonds and $\pi-\pi^*$ [1,64,65]. Furthermore, the N1 s high resolution spectrum of chitosan microspheres before calcination exhibits a major peak around 401.5 eV which comes from the non-protonated amine

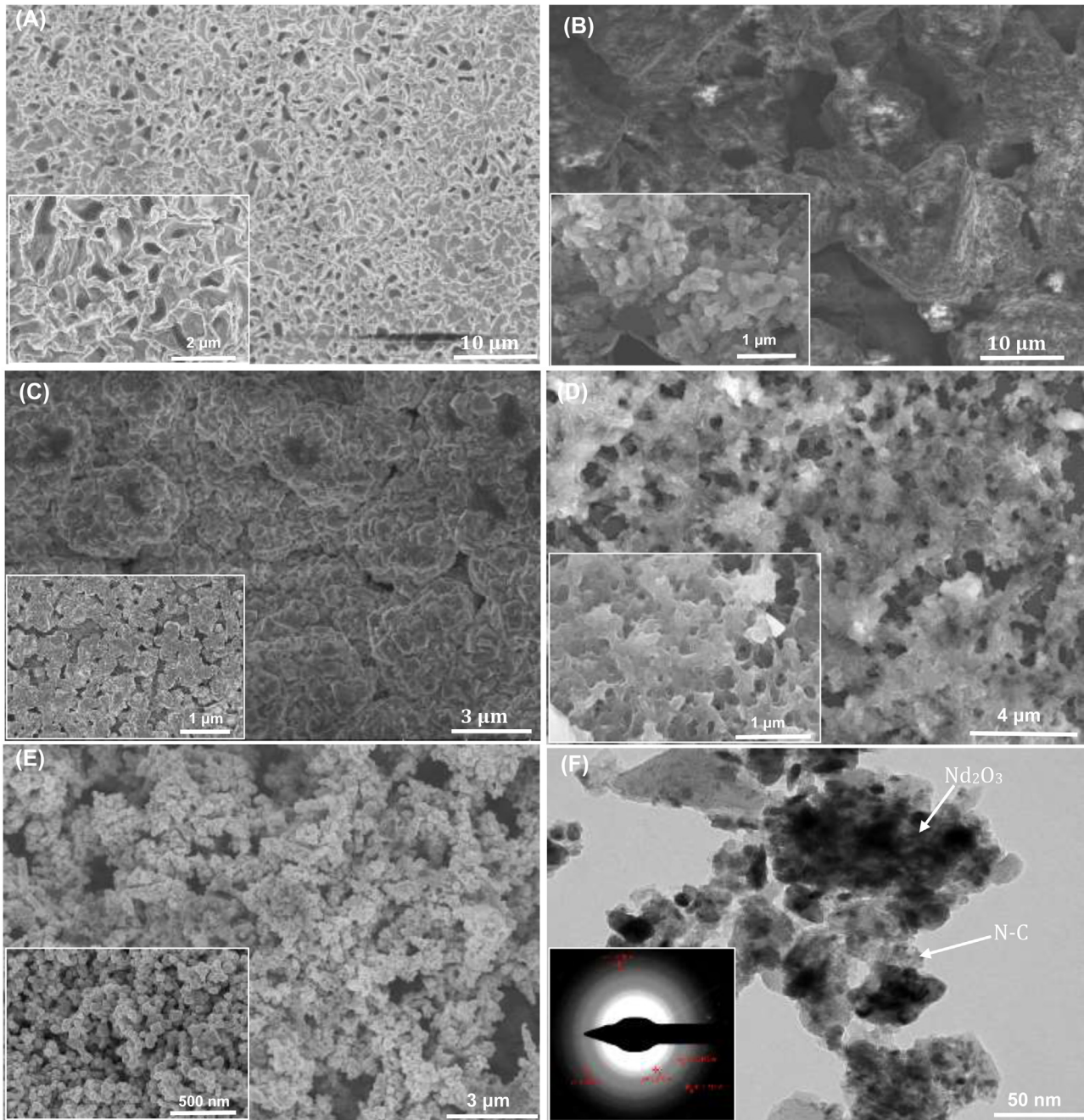


Fig. 1. SEM images of (A) nano-CS, (B) N—C, (C) Nd₂O₃, (D) nano-CS-Nd(OH)₃ and (E) Nd₂O₃/N—C catalysts (F) TEM of Nd₂O₃/N—C. N.b., N—C, Nd₂O₃ and Nd₂O₃/N—C are referring to the annealed nano-CS, Nd(OH)₃ and nano-CS-Nd(OH)₃ at 700 °C under nitrogen atmosphere for 3 h, respectively.

or amide ($-\text{NH}_2$ and $-\text{NH}-$) and the minor peak around 402.8 eV occurred due to the protonated amine (NH_3^+ , Fig. 2C) [60,66]. Interestingly, the N1 s spectrum of the annealed chitosan at 700 °C (N—C) reveals a doublet peak that can be resolved into four peaks originating from different nitrogen states, including pyridinic N (399 eV, 78%), pyrrolic N (400.7, 5%), graphitic N (402 eV, 15%) and pyridinic N-oxide (403.1 eV, 2%), suggesting the formation of nitrogen doped carbons during the thermal decomposition of chitosan structure (Fig. 2D) [67–69].

The same observation of C1 s and N1 s of the nano-CS-Nd(OH)₃ before calcination was obtained, but the binding energies of C—O, O—C—O and O=C—O were shifted towards higher binding energies and the N1 s is shifted as well to higher binding energy, besides their relative contents were changed after adsorption of neodymium

(data not shown) [52]. This observation indicates that ether, alcoholic, carboxylate and amine groups of chitosan get involved in the neodymium adsorption in which the oxygen and nitrogen atoms donate electrons to metal ions and thus the electron density at the adjacent carbon atom decreases [70,71]. Surprisingly, the N1 s high resolution spectrum of the Nd₂O₃/N—C (calcined nano-CS-Nd(OH)₃ at 700 °C) shows six different deconvoluted peaks which were attributed to various nitrogen types, such as pyridinic N (399 eV, 12%), quaternary N (400 eV, 22%), pyrrolic N (400.7, 17%), graphitic N (402 eV, 36%), pyridinic N-oxide (403.1 eV, 11%) and O—Nd—N ring (404 eV, 2%) indicating the doping of Nd₂O₃ as well.

Nd₂O₃/N—C has a greater amount of doped nitrogen (~18%) compared to N—C (~10%), suggesting that CS can be used to synthesize N-doped carbon and N-doped metal oxide (Fig. 2E)

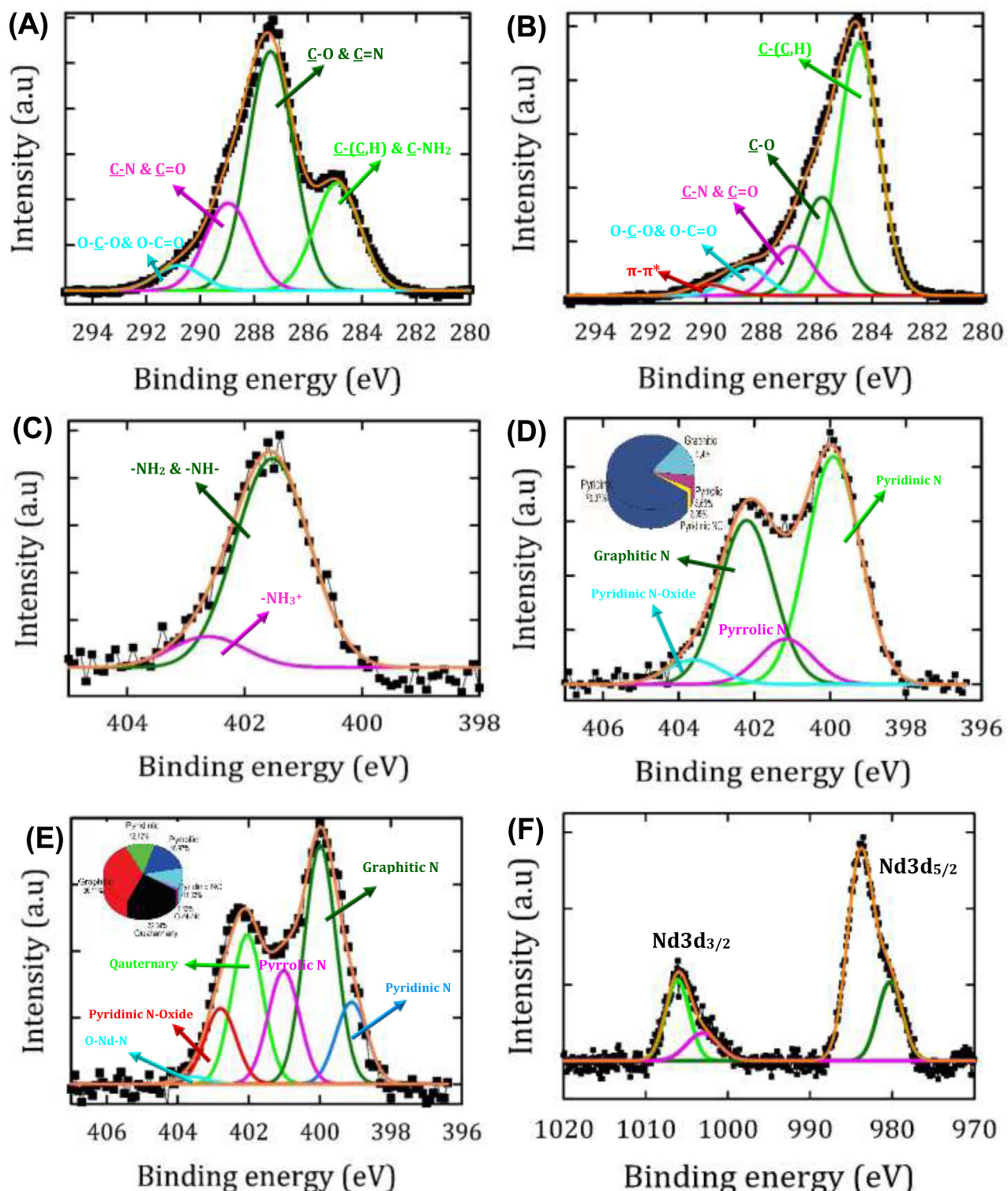


Fig. 2. High resolution XPS spectra of C1 s and N1 s chitosan before (A, C) and after calcination; N—C (B,D), N1 s (E) and Nd3d (F) spectra of Nd₂O₃/N—C.

[1,72]. In order to verify that CS can be used as a nitrogen dopant source to synthesize nitrogen-doped metal oxides (e.g., N—Nd₂O₃), the chitosan-neodymium hydroxide composite (nano-CS-Nd(OH)₃) was first prepared as described in the experimental part, but calcined at 800 °C under air instead of nitrogen. This resulted in the formation of nitrogen doped neodymium oxide (N—Nd₂O₃) without any carbon as indicated from its respective EDS, XPS and sample color analyses (Fig. S4), wherein no carbon

peak was observed (i.e., only Nd, O and N peaks were observed). Moreover, the sample color became pale purple which is characteristic for pure Nd₂O₃ compared to its black color in case of annealing under nitrogen atmosphere (Fig. S4D). Moreover, the N1 s high resolution spectrum of this sample (N—Nd₂O₃) exhibited only one peak around 403 eV attributed to the O-Nd-N ring (Fig. S4B). In contrast, Fig. 2F shows the high-resolution spectrum of Nd3d of the Nd₂O₃/N—C. As clearly seen in Fig. 2F, the peaks of Nd3d_{5/2}

and Nd $3d_{3/2}$ core levels are found to be centered at 983 eV and 1006 eV, respectively, which can be considered as contributions from Nd $^{3+}$ in Nd $_2$ O $_3$ when compared with literature data[73–75]. The XPS overall spectra of the calcined (N–C and Nd $_{2O_3$ /N–C) and un-calcined pure Nd $_2$ O $_3$, CS and nano-CS-Nd(OH) $_3$ catalysts are presented in Fig. S4E. Additionally, Fig. S5 shows Raman spectra of N–C and Nd $_{2O_3$ /N–C, both catalysts exhibit G- and D- bands which can be deconvoluted into five different peaks assigned as follows: G-band (\sim 1588 cm $^{-1}$) is attributed to the strongly coupled carbons in the hexagonal sheet in-plane displacement. The other four peaks represent the D-bands, where peaks at 1322 cm $^{-1}$ and 1650 cm $^{-1}$ are assigned for D1 and D2 representing the disorder in the structure, respectively, and the peaks at 1520 cm $^{-1}$ and 1200 cm $^{-1}$ are attributed to D3 and D4 which are assigned to the interstitial defects or amorphous sp 2 -bonded carbons, besides C–C and C=C stretching vibrations of polyene-like structure [76], respectively.

3.2. Activity towards ORR and OER

To assess the electrocatalytic activities of the as-prepared catalysts for ORR, they were loaded first onto the GC electrodes with the same mass loading and then their CVs were investigated in O $_2$ versus N $_2$ -saturated 0.1 M KOH aqueous solution, data are presented in Fig. 3A. As clearly seen in this figure, the as-prepared catalysts exhibited a well-defined cathodic peak corresponding to the oxygen reduction in O $_2$ -saturated solution (Fig. 3A-soild lines), while no cathodic peak could be observed in their respective CVs in N $_2$ -saturated solution. This clearly indicates their electrocatalytic activity for ORR. Moreover, the nano-CS (Fig. 3A-curve a) and pure calcined Nd $_2$ O $_3$ (Fig. 3A-curve b) modified GC electrodes showed poor ORR activities. Remarkably, the calcined nano-CS (assigned as N–C, Fig. 3A-curve c) and calcined nano-CS-Nd(OH) $_3$ (assigned as N–CNd $_2$ O $_3$, Fig. 3A-curve d) modified GC electrodes exhibited a significantly more positive ORR onset potential concurrent with higher cathodic currents, suggesting the formation of nitrogen-doped carbon-neodymium oxide hybrid material after annealing.

On the other hand, Nd $_{2O_3$ /N–C catalyst (Fig. 3A-curve d) showed a superior ORR activity with the highest ORR onset potential (-0.04 V vs. SCE) compared to N–C (-0.12 V, Fig. 3A-curve c) and pure Nd $_2$ O $_3$ (-0.21 V, Fig. 3A-curve b) electrodes indicating synergistic ORR catalytic activity of Nd $_2$ O $_3$ and N–C in their hybrid. Rotating-disk electrode (RDE) LSVs measurements were recorded to evaluate the kinetics and gain further insight into the catalytic activity of the as-prepared electrodes for ORR in alkaline (Fig. 3B) and acidic medium (Fig. 3C) in comparison with the commercial Pt/C catalyst. Indeed, as clearly shown in Fig. 3B, Nd $_{2O_3$ /N–C catalyst (curve f) has a more positive half-wave potential ($E_{1/2} \sim -0.08$ V) with a higher limiting current density for ORR compared to Nd(OH) $_3$ (curve a, $E_{1/2} \sim -0.28$ V), nano-CS (curve b, $E_{1/2} \sim -0.26$ V), nano-CS-Nd(OH) $_3$ (curve c, $E_{1/2} \sim -0.25$ V), pure Nd $_2$ O $_3$ (curve d, $E_{1/2} \sim -0.18$ V), N–C (annealed nano-CS, curve e, $E_{1/2} \sim -0.14$ V) and the commercial Pt/C (curve g, $E_{1/2} \sim -0.11$ V) electrodes.

The same behavior is observed in acidic medium (Fig. 3C), whereas the Nd $_{2O_3$ /N–C catalyst (Fig. 3C-curve f) displays a comparable activity to that of the commercial Pt/C electrode (Fig. 3C-curve g) and a much better activity compared to Nd $_2$ O $_3$ (curve a), nano-CS (curve b), nano-CS-Nd(OH) $_3$ (curve c), pure Nd $_2$ O $_3$ (curve d) and N–C (curve e). The LSVs of the as-prepared catalysts were recorded at different rotation speeds in order to evaluate the number of transferred electrons (n) based on Koutecky-Levich (K-L) plots. The electron transfer number (n) was estimated to be ~ 4.1 for N–C catalyst (Fig. 3 D) and ~ 3.9 for the Nd $_{2O_3$ /N–C catalyst (Fig. 3 E) from the slopes of K-L plots [3,16], suggesting an efficient four-electron (4e $^-$) dominated oxy-

gen reduction process similar to that of a high-quality commercial Pt/C catalyst (see Fig. S6 A). Interestingly, a four-electron reduction process will reduce the amount of formed hydrogen peroxide resulting in a considerable stability. In contrast, the pure Nd $_2$ O $_3$ and un-calcined nano-CS modified GC electrodes exhibited a lower ORR activity with calculated electron transfer numbers of ~ 2.4 and ~ 2.6 , respectively, indicating the dominant two-electron reduction pathway with a higher hydrogen peroxide yield (Fig. S6 (B&C)). The admirable ORR activities of Nd $_{2O_3$ /N–C (~ 45 mV/decade, Fig. 3F-curve e) and N–C (~ 46 mV/decade, Fig. 3F-curve c) catalysts could be attributed to their lower Tafel slopes at lower overpotential than that of the commercial Pt/C (Fig. 3F-curve d), nano-CS (Fig. 3F-curve a) and pure Nd $_2$ O $_3$ (Fig. 3F-curve b). Interestingly, Tafel plots of the as-prepared catalysts and the commercial Pt/C electrodes show two different regions with two different slopes at low and higher current densities (the Tafel slopes of both regions are written in Fig. 3F) attributed to the Temkin and Langmuir oxygen adsorption, respectively. The lower Tafel slopes of N–C and Nd $_{2O_3$ /N–C suggest that the oxygen adsorption on them is more energetically favorable [1,77,78]. Additionally, the smaller Tafel slope of Nd $_{2O_3$ /N–C in the higher current density region compared to the N–C indicates the existence of Nd $_2$ O $_3$ which could result in a low Tafel slope of the Nd $_{2O_3$ /N–C catalyst. Furthermore, the low Tafel slopes of N–C and Nd $_{2O_3$ /N–C catalysts could be attributed to their nitrogen doped structure, whereas the nitrogen doping induced charge delocalization and high hydrophilicity which are energetically favorable for oxygen adsorption (i.e. their N-doped structure resulted in a lower oxygen dissociation and adsorption energy leading to a higher activity [1,79,80]). In addition, the N–C and Nd $_{2O_3$ /N–C have the same Tafel slope at low current density, that might suggest that the Nd $_{2O_3$ /N–C Tafel slope at low current density is determined by the N–C.

To investigate the electrode kinetics of the different as-prepared catalysts, EIS (Nyquist plots) measurements were performed at -0.2 V, data are presented in Fig. 4A. As clearly revealed from the Nyquist plots (Fig. 4A), Nd $_{2O_3$ /N–C exhibits a smaller ORR charge transfer resistance ($R_{ct} \sim 55$ ohm, curve f) compared to N–C ($R_{ct} \sim 91$ ohm, curve e), calcined pure Nd $_2$ O $_3$ ($R_{ct} \sim 189$ ohm, curve d), nano-CS-Nd(OH) $_3$ ($R_{ct} \sim 450$ ohm, curve c), pure un-calcined Nd $_2$ O $_3$ ($R_{ct} \sim 4000$ ohm, curve b) and nano-CS ($R_{ct} \sim 6500$ ohm, curve a) catalysts. The lower charge transfer resistance of the Nd $_{2O_3$ /N–C will markedly facilitate the process for shuttling the charges from the electrocatalysts to oxygen. This might be attributed to its nitrogen doped structure and the synergistic effect between the N–C and Nd $_2$ O $_3$ nanostructured material. As clearly seen in Fig. 4B, Nd $_{2O_3$ /N–C remains highly efficient for ORR with only a slight decrease in its activity in O $_2$ -saturated 0.5 M KOH solution after 1000 continuous cycles with a scan rate of 5 mV/s compared with the momentous loss in the activity of both N–C (see Fig. S7A) and commercial Pt/C (see Fig. S7B) electrodes. For instance, the activity of Nd $_{2O_3$ /N–C catalyst for ORR was reduced by only 3% from its original activity over the course of more than 8 h of contentious ORR measurements (see inset of Fig. 4B-curve a) compared with N–C ($\sim 20\%$, Fig. 4B inset-curve b) and commercial Pt/C ($\sim 50\%$, Fig. 4B inset-curve a) electrodes, as estimated from their respective chronoamperometric responses (i-t) in O $_2$ -saturated solution of 0.5 M KOH at -0.2 V.

It is well-known that the poor stability of the Pt/C catalyst originates from surface oxides, dissolution and aggregation of the Pt nanoparticles after the oxidative degradation of the carbon support, especially in alkaline medium. We believe that the nitrogen doped and composite structure of our proposed catalyst (where the Nd $_2$ O $_3$ is embedded inside the chitosan matrix and then calcined to produce nitrogen doped carbon-neodymium oxide hybrid material) hinders the dissolution and aggregation of the active sites resulting in a better durability. The lack in catalyst durability

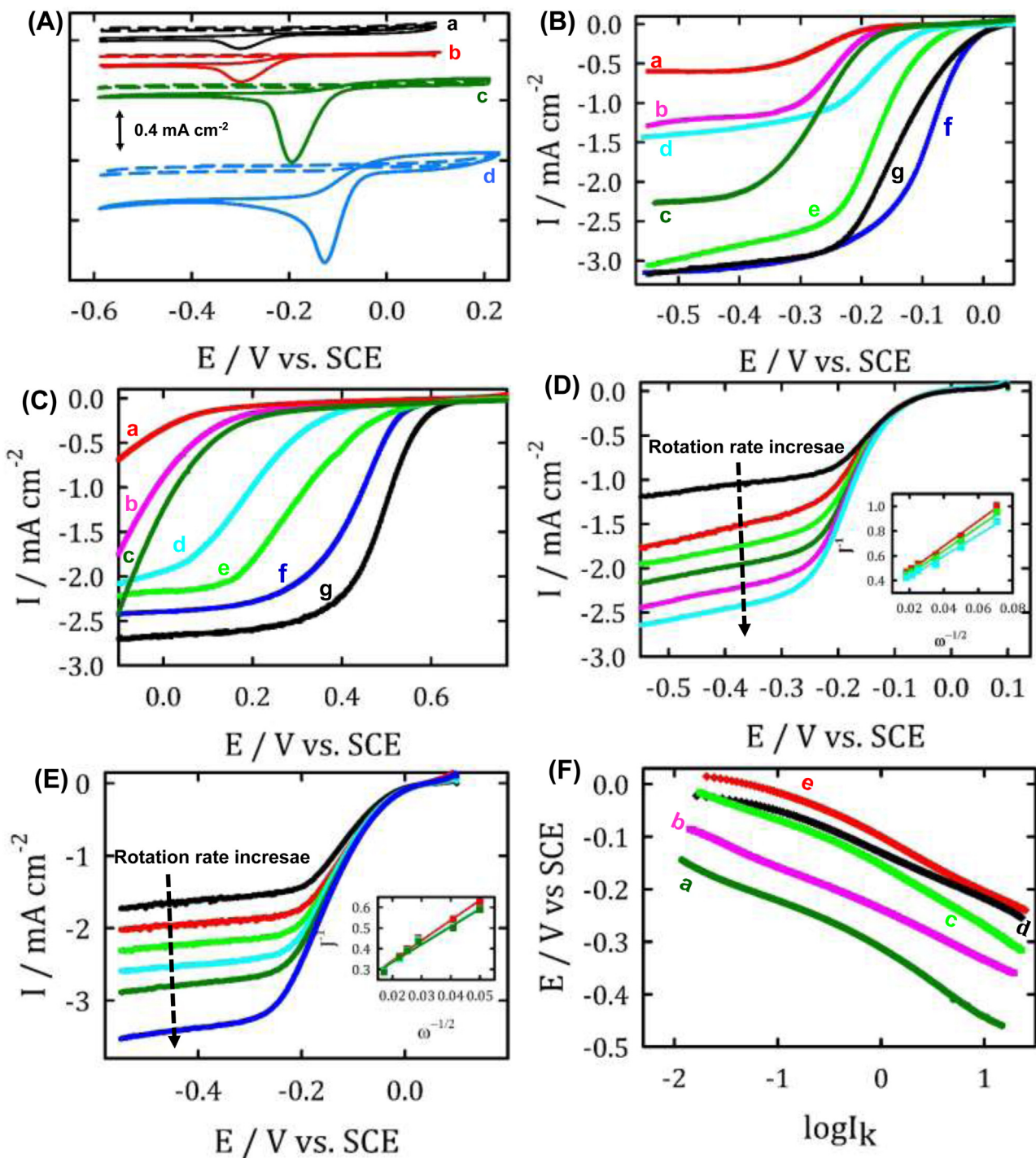


Fig. 3. (A) CVs of nano-CS (curve a), pure Nd₂O₃ (curve b), N-C (curve c) and Nd₂O₃/N-C (curve d) in O₂ (solid-lines)-and N₂ (dashed-lines)-saturated 0.1 M KOH solution, (B) LSVs of nano-CS (curve a), nano-CS-Nd(OH)₃ (curve b), pure Nd(OH)₃ (curve c), pure Nd₂O₃ (curve d), N-C (curve e), Nd₂O₃/N-C (f) and commercial Pt/C (curve g) in O₂-saturated 0.1 M KOH solution at rotation rate of 1600 rpm, (C) LSVs of nano-CS (curve a), nano-CS-Nd(OH)₃ (curve b), Nd(OH)₃ (curve c), Nd₂O₃ (curve d), N-C (curve e), Nd₂O₃/N-C (curve f) and commercial Pt/C (curve g) in O₂-saturated 0.1 M HClO₄ solution at rotation rate of 1600 rpm, (D, E) RDE voltammograms and the corresponding Koutecky-Levich (K-L) plots of the N-C (D) and Nd₂O₃/N-C (E) at various rotation rates in O₂-saturated 0.1 M KOH solution (typically; 200, 400, 800, 1600, 2200 and 3000 rpm), and (F) Tafel plots of nano-CS (curve a), pure Nd₂O₃ (curve b), N-C (curve c) and Nd₂O₃/N-C (curve e).

is one of the major challenges in alkaline fuel cells commercialization, thus the high activity and durability of the Nd₂O₃/N-C make it a promising catalyst for ORR and other important catalytic reactions in alkaline medium. Furthermore, the effect of several anodic fuels crossover on the activity and durability of Nd₂O₃/N-C and commercial Pt/C electrodes for ORR in alkaline medium was investigated using chronoamperometry. As clearly demonstrated

in Fig. 4C, the original ORR current of the Pt/C catalyst is affected dramatically by the addition of 1 M of the above mentioned anode fuels methanol, ethanol, ethylene glycol and propanol, indicating their oxidation, while in case of formic acid the significant decrease of the ORR current is most likely due to the formation of CO from the non-faradaic dissociation of formic acid at the Pt surface deactivating/poisoning the majority of the active Pt sites (N.B., CO can be

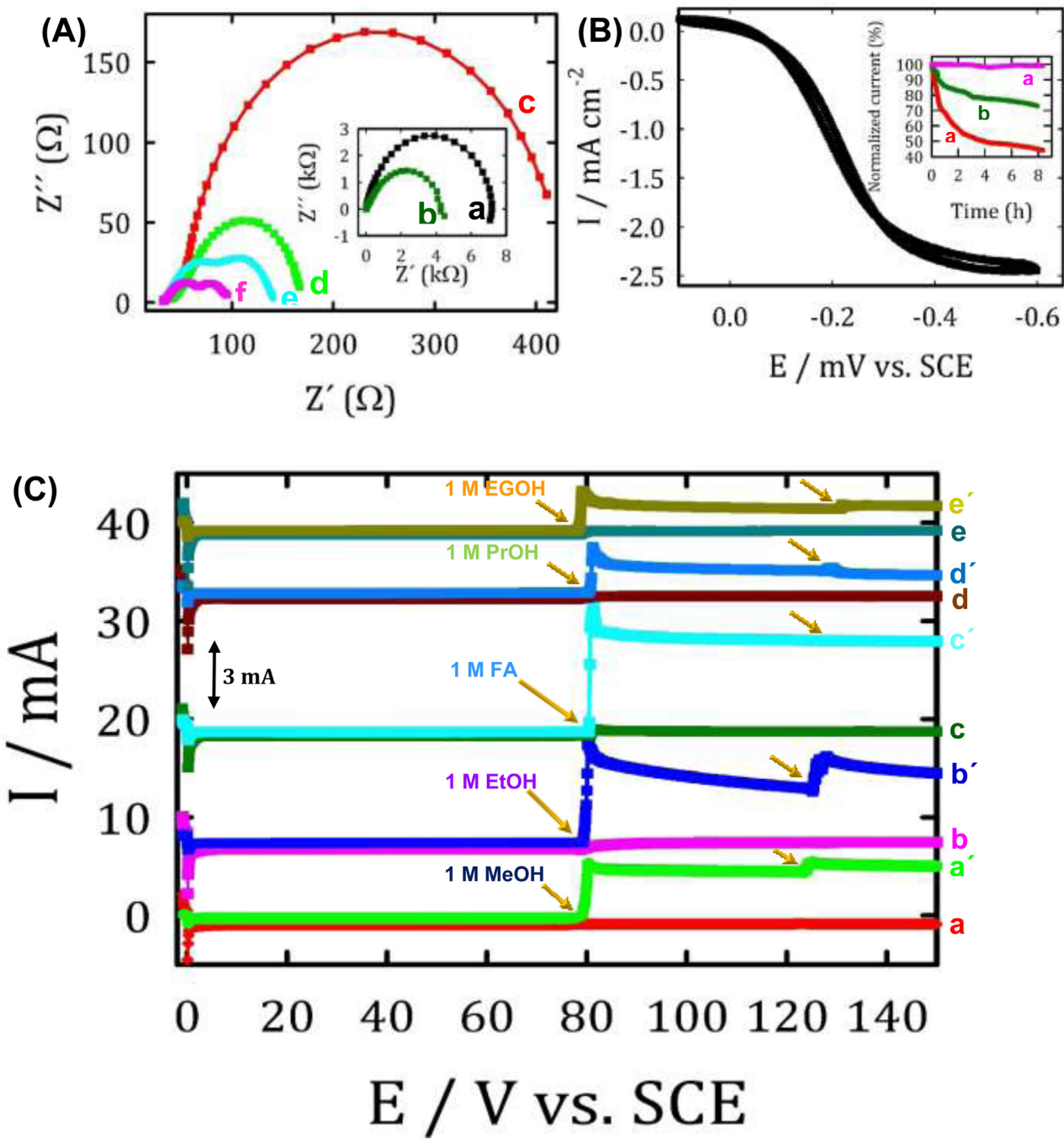


Fig. 4. (A) Nyquist plots obtained at (a) nano-CS, (b) Nd(OH)₃, (c) nano-CS-Nd(OH)₃, (d) Nd₂O₃, (e) N-C and (f) Nd₂O₃/N-C at -0.2 V in 0.1 M KOH , (B) contentious LSVs obtained at Nd₂O₃/N-C in O_2 -saturated 0.5 M KOH solution (inset shows the variation of normalized current of Pt/C (a), N-C (b) and Nd₂O₃/N-C (c) with time) and (C) Amperometric response of Nd₂O₃/N-C (a-e) and Pt/C (a'-e') electrodes during measurement 1 M of methanol (MeOH- curves (a, a')), ethanol (EtOH- curves (b, b')), formic acid (FA-curves (c, c')) and 2-propanol (PrOH-curves (d, d')) were added (arrows show the impurity additions).

produced from formic acid dehydration at open circuit potential, this fact is evidenced in our previous studies [81,82]. In sharp contrast, the chronoamperometric response of Nd₂O₃/N-C catalyst towards these fuels shows no change of the ORR current. Indeed, the Nd₂O₃/N-C catalyst is a promising candidate for the various types of polymer electrolyte membrane fuel cells, such as direct methanol fuel cells, direct formic acid fuel cells, direct ethanol fuel cells etc.

Another serious issue hindering commercialization is the decline of the catalyst efficiency in the presence of minute amounts of organic, hydrocarbon and/or inorganic contaminants entering

the cell with air or *in-situ* generated from the degradation of the different fuel cell components (e.g., tubes, gaskets, etc) [8,19,83–86]. Actually, impurities stemming from the degradation of fuel cell plants components have a severe poisoning effect on the fuel cell performance and durability. Thus, this study and our previous work [8,19,83–86] in this field are aimed to recognize the poisoning and/or enhancement mechanism of the various types of impurities which would help fuel cell industry in reducing the overall fuel cell cost by lowering the balance of plant component and electrode material costs without sacrificing the fuel cell efficiency. Fig. 5 shows the effect of acrylonitrile on the electrocatalytic activity of

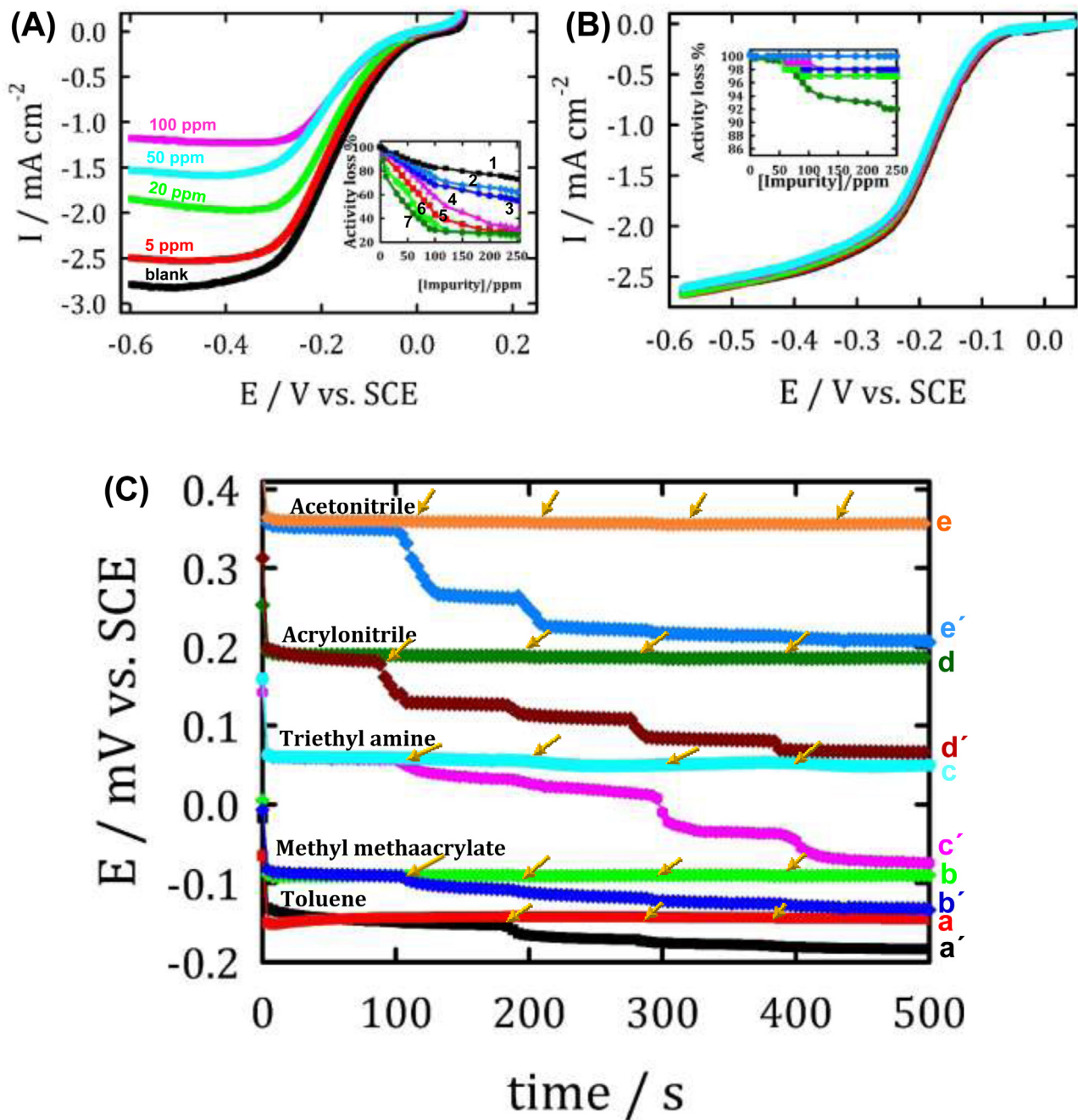


Fig. 5. LSVs obtained at (A) Pt/C and (B) Nd₂O₃/N-C in the existence of various acrylonitrile concentrations in 0.1 M KOH (inset of each figure shows the variation of the activity loss with various HCs impurities concentration (typically; (1) acetonitrile, (2) acrylonitrile, (3) triethyl amine, (4) vinyl acetate, (5) acetamide, (6) methyl methacrylate and (7) toluene, same colors are used for Fig. 5A and Fig. 5B)) and (C) Amperometric response of Nd₂O₃/N-C (a-e) and Pt/C (a'-e') electrodes during measurement successive 50 ppm of various HCs impurities were added (arrows show the additions) (typically; Toluene (a, a'), methylmethacrylate (b, b'), triethyl amine (c, c'), acrylonitrile (d, d') and acetonitrile (e, e')).

commercial Pt/C (Fig. 5A) and Nd₂O₃/N-C (Fig. 5B) towards ORR in alkaline medium. As clearly revealed from Fig. 5A, the existence of a minute amount of contaminant can result in a large negative shift of the onset potential and the half-wave potential of ORR with the extent depending on the acrylonitrile concentration concurrent with a markedly lowered ORR limiting current density of Pt/C electrodes. However, the existence of acrylonitrile has no effects on the activity of the Nd₂O₃/N-C catalyst (Fig. 5B). For instance, the presence of 50 ppm of acrylonitrile resulted in 60% loss of the ORR limiting current and 100 mV negative shift of the half-wave potential of the Pt/C catalyst compared with only 1% decrease and 5 mV negative shift of ORR at Nd₂O₃/N-C catalyst.

The same behavior was obtained in the presence of other hydrocarbon impurities, such as acetonitrile, trimethylamine, vinyl acetate, acetamide and methyl methacrylate, but with different poisoning extent depending on the nature of the electrode and the type of impurity, the results are summarized in the insets of Fig. 5A and Fig. 5B. Furthermore, Fig. 5C shows the amperometric responses of Pt/C and Nd₂O₃/N-C in O₂-saturated 0.1 M KOH solution at -0.2 V and rotation rate of 1600 rpm with the successive addition of 50 ppm of various hydrocarbon impurities. As clearly demonstrated from this figure, the addition of these impurities resulted in a significant decrease of the ORR current of Pt/C with various extent depending on the nature of the impurity (the

order of activity loss as following: acetonitrile > acrylonitrile > triethyl amine > vinyl acetate > acetamide > methyl methacrylate > toluene), while they have no effect on the Nd₂O₃/N–C catalyst indicating the high tolerance of our catalyst against various types of impurities compared with the low tolerance of the commercial Pt/C catalyst. In our previous work [8,81,83,84], the surprising enhancement effect of the above mentioned hydrocarbon impurities on the Pt/C and nano-CS-NiOOH electrocatalytic activities towards formic acid oxidation (essential anodic reaction of direct formic acid fuel cells) and glucose electrooxidation (anodic reaction of glucose fuel cells) is reported.

Herein, we introduce a Pt-free catalyst with a very high activity, durability and poisoning tolerance for crossover and various impurities for ORR (cathodic reaction of fuel cells). Based on these studies, one might build fuel cell components from very cheap materials, and even if these cheap materials decompose, the resulting impurities will increase the activity and durability of our proposed catalysts.

Lastly, we investigated the activity and durability of our proposed catalysts for the water oxidation regime (oxygen evolution reaction; OER). The OER and ORR are investigated at the same electrodes in 0.1 M KOH by extending the potential of the as-prepared electrodes to 1.2 V vs. SCE. As seen in Fig. 6A, Nd₂O₃/N–C catalyst achieved higher OER currents compared to the commercial Pt/C, nano-CS, pure Nd₂O₃ (curve c) and N–C catalysts. Additionally, the Nd₂O₃/N–C catalyst exhibited a very high durability as indicated from inset of Fig. 6A with a smaller Tafel slope compared with commercial Pt/C and the other proposed electrodes as shown in Fig. 6B. Since our as-prepared catalyst exhibits enhanced ORR activity and durability, single cell tests were performed by using N–C and Nd₂O₃/N–C as the cathode catalyst with loading of 0.3 mg cm⁻² and Pt/C as the anode with loading 0.1 mg cm⁻² in a membrane electrode assembly (MEA) having an active area of 8.7 cm⁻² (data represented in Fig. 6C). As revealed in this figure, Nd₂O₃/N–C delivers a higher maximum power density (287 mW cm⁻²) and current density 570 mA cm⁻² at 0.6 V compared to that of N–C with the same loading level (200 mW cm⁻² and 442 mA cm⁻²). These obtained values are better or comparable to that of recently reported cell performance data of the Pt-free electrocatalysts indicating the brilliant intrinsic activity of our proposed catalyst [87–89]. However, the obtained fuel cell performance of our as-prepared catalyst is less than that of the commercial Pt/C (585 mW cm⁻², Fig. S8). But considering the cost, availability, durability and facile synthesis method with respect to the commercial Pt/C, N–C and N–CNd₂O₃ can be considered as a potential alternative cathode catalyst for PEMFC applications. It is worthy to mention here that this is the first test only whereas no parameters were optimized to obtain a higher performance.

4. Conclusions

We have successfully converted chitosan which is obtained from crustacean's shells to a highly active bifunctional nitrogen-doped carbon (N–C) for ORR and OER. N-doped carbon-Nd₂O₃ hybrid (Nd₂O₃/N–C) was prepared via the thermal decomposition of the embedded chitosan microspheres with neodymium hydroxide. However, pure Nd₂O₃ or chitosan alone have little activity for ORR, their hybrid nanostructure (Nd₂O₃/N–C) shows outstanding electrocatalytic activity and durability as a bifunctional oxygen reduction and evolution reaction catalyst. Nd₂O₃/N–C catalyst exhibits a higher catalytic activity, durability and poisoning tolerance against various anodic fuels crossover such as methanol, ethanol and formic acid compared to the fresh commercial Pt/C catalyst. Additionally, it has a higher tolerance for hydrocarbon impurities, in-situ generated during the fuel cell operation from

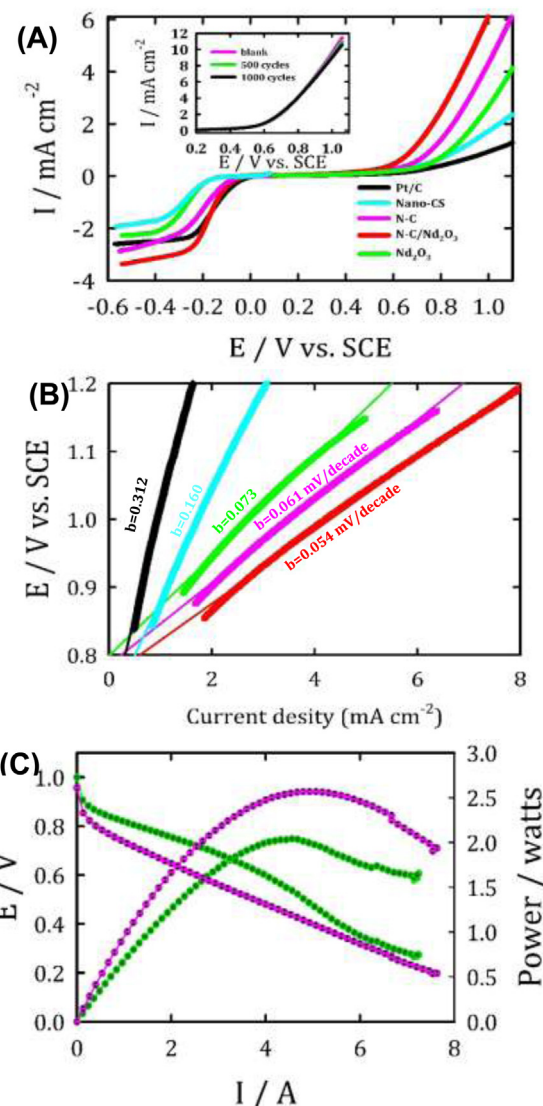


Fig. 6. (A) oxygen electrode activities within OER and ORR potential window of nano-CS, Nd₂O₃, N–C, Nd₂O₃/N–C and Pt/C in 0.1 M KOH O₂-saturated solution (inset shows LSVs of OER obtained at Nd₂O₃/N–C after 500 and 1000 cycles in 0.1 M KOH solution with scan rate of 5 mV/s), (B) Tafel plots of OER currents (the same electrodes and colors of Fig. A were used), and (C) single cell polarization curves tested at 80 °C of PEMFCs with N–C (light green lines) and Nd₂O₃/N–C (pink lines, 0.3 mg cm⁻²) as cathode and Pt/C (0.1 mg cm⁻²) as anode catalysts. (For interpretation of the references to colour in this figure legend, the reader is referred to the web version of this article.)

the degradation of various fuel cell components. Considering the cost, availability, durability and facile synthesis method of N–C and Nd₂O₃/N–C hybrid materials, our proposed catalysts can be considered as potential alternative cathode catalysts for PEMFC applications and open up a new horizon for the world-wide commercialization of fuel cells and metal-air batteries.

Acknowledgement

This work was financially supported by Alexander von Humboldt Foundation (AvH). Guma A. El-Nagar is grateful for a fellowship from the AvH.

Appendix A. Supplementary data

Supplementary data associated with this article can be found, in the online version, at <http://dx.doi.org/10.1016/j.apcatb.2017.05.030>.

References

- [1] Z.-J. Jiang, Z. Jiang, *Sci. Rep.* 6 (2016) 27081.
- [2] J. Zhang, Z. Zhao, Z. Xia, L. Dai, *Nat. Nano* 10 (2015) 444–452.
- [3] Y. Liang, Y. Li, H. Wang, J. Zhou, J. Wang, T. Regier, H. Dai, *Nat. Mater.* 10 (2011) 780–786.
- [4] N.S. Lewis, D.G. Nocera, *Proc. Natl. Acad. Sci.* 103 (2006) 15729–15735.
- [5] G.A. El-Nagar, I. Derr, A. Fetyan, C. Roth, *Appl. Catal. B: Environ.* 204 (2017) 185–199.
- [6] M.S. El-Deab, G.A. El-Nagar, A.M. Mohammad, B.E. El-Anadolli, *J. Power Sources* 286 (2015) 504–509.
- [7] G.A. El-Nagar, A.F. Darweesh, I. Sadiek, *Electrochim. Acta* 215 (2016) 334–338.
- [8] G.A. El-Nagar, C. Roth, *Phys. Chem. Chem. Phys.* 19 (2017) 2537–2548.
- [9] E.H. Yu, X. Wang, U. Krewer, L. Li, K. Scott, *Energy Environ. Sci.* 5 (2012) 5668–5680.
- [10] Z. Chen, D. Higgins, A. Yu, L. Zhang, J. Zhang, *Energy Environ. Sci.* 4 (2011) 3167–3192.
- [11] A.A. Gewirth, M.S. Thorum, *Inorg. Chem.* 49 (2010) 3557–3566.
- [12] R.M. Yadav, J. Wu, R. Kochandria, L. Ma, C.S. Tiwary, L. Ge, G. Ye, R. Vajtai, J. Lou, P.M. Ajayan, *ACS Appl. Mater. Interfaces* 7 (2015) 11991–12000.
- [13] Z.-J. Jiang, Z. Jiang, *ACS Appl. Mater. Interfaces* 6 (2014) 19082–19091.
- [14] G. Chen, S.R. Bare, T.E. Mallouk, *J. Electrochem. Soc.* 149 (2002) A1092–A1099.
- [15] B.P. Vinayan, T. Diermant, R.J. Behm, S. Ramaprabhu, *RSC Adv.* 5 (2015) 66494–66501.
- [16] N. Wu, Y. Wang, Y. Lei, B. Wang, C. Han, Y. Gou, Q. Shi, D. Fang, *Sci. Rep.* 5 (2015) 17396.
- [17] Z. Zhang, J. Liu, J. Gu, L. Su, L. Cheng, *Energy Environ. Sci.* 7 (2014) 2535–2558.
- [18] J. Shui, M. Wang, F. Du, L. Dai, *Sci. Adv.* 1 (2015).
- [19] M.S. El-Deab, F. Kitamura, T. Ohsaka, *J. Electrochem. Soc.* 160 (2013) F651–F658.
- [20] D.G. Nocera, *Inorg. Chem.* 48 (2009) 10001–10017.
- [21] A.J. Bard, M.A. Fox, *Acc. Chem. Res.* 28 (1995) 141–145.
- [22] T. Reier, M. Oezaslan, P. Strasser, *ACS Catal.* 2 (2012) 1765–1772.
- [23] Y. Shao, S. Park, J. Xiao, J.-G. Zhang, Y. Wang, J. Liu, *ACS Catal.* 2 (2012) 844–857.
- [24] I. Katsounaros, S. Cherevko, A.R. Zeradjanin, K.J.J. Mayrhofer, *Angew. Chem. Int. Ed.* 53 (2014) 102–121.
- [25] J. Masa, W. Xia, I. Sinev, A. Zhao, Z. Sun, S. Grützke, P. Weide, M. Muhler, W. Schuhmann, *Angew. Chem. Int. Ed.* 53 (2014) 8508–8512.
- [26] Y. Zhao, K. Kamiya, K. Hashimoto, S. Nakanishi, *J. Phys. Chem. C* 119 (2015) 2583–2588.
- [27] R. Bashyam, P. Zelenay, *Nat* 443 (2006) 63–66.
- [28] Y. Liu, T.G. Kelly, J.G. Chen, W.E. Mustain, *ACS Catal.* 3 (2013) 1184–1194.
- [29] Y. Zhong, X. Xia, F. Shi, J. Zhan, J. Tu, H.J. Fan, *Adv. Sci.* 3 (2016) 1500286–1500314.
- [30] C. Zhu, H. Li, S. Fu, D. Du, Y. Lin, *Chem. Soc. Rev.* 45 (2016) 517–531.
- [31] S. Dou, X. Li, L. Tao, J. Huo, S. Wang, *Chem. Comm.* 52 (2016) 9727–9730.
- [32] L. Tao, Q. Wang, S. Dou, Z. Ma, J. Huo, S. Wang, L. Dai, *Chem. Comm.* 52 (2016) 2764–2767.
- [33] Y. Wang, D. Liu, Z. Liu, C. Xie, J. Huo, S. Wang, *Chem. Comm.* 52 (2016) 12614–12617.
- [34] O. Vaughan, *Nat. Nano* 351 (2016) 361–365.
- [35] L. Qu, Y. Liu, J.-B. Baek, L. Dai, *ACS Nano* 4 (2010) 1321–1326.
- [36] L. Feng, L. Yang, Z. Huang, J. Luo, M. Li, D. Wang, Y. Chen, *Sci. Rep.* 3 (2013) 3306.
- [37] Y. Li, W. Zhou, H. Wang, L. Xie, Y. Liang, F. Wei, J.-C. Idrobo, S.J. Pennycook, H. Dai, *Nat. Nano* 7 (2012) 394–400.
- [38] L. Feng, Y. Chen, L. Chen, *ACS Nano* 5 (2011) 9611–9618.
- [39] Y.-P. Lin, Y. Ksari, J. Prakash, L. Giovanelli, J.-C. Valmalette, J.-M. Themlin, *Carbon* 73 (2014) 216–224.
- [40] H. Huang, G. Luo, L. Xu, C. Lei, Y. Tang, S. Tang, Y. Du, *Nanoscale* 7 (2015) 2060–2068.
- [41] Z. Xing, Z. Ju, Y. Zhao, J. Wan, Y. Zhu, Y. Qiang, Y. Qian, *Sci. Rep.* 6 (2016) 26146.
- [42] W. Shen, W. Fan, J. Mater. Chem. A 1 (2013) 999–1013.
- [43] X.-F. Li, K.-Y. Lian, L. Liu, Y. Wu, Q. Qiu, J. Jiang, M. Deng, Y. Luo, *Sci. Rep.* 6 (2016) 23495.
- [44] N. Yan, X. Chen, *Nat* 524 (2015) 155–158.
- [45] X. Chen, H. Yang, N. Yan, *Chem. – A Eur. J.* 22 (2016) 13402–13421.
- [46] Y. Gao, X. Chen, J. Zhang, N. Yan, *Chem. Plus. Chem.* 80 (2015) 1556–1564.
- [47] C. Dhandapani, R. Narayanasamy, S.N. Karthick, K.V. Hemalatha, S. Selvam, P. Hemalatha, M.S. Kumar, S.D. Kirupha, H.-J. Kim, *Optik – Int. J. Light Electron Optics* 127 (2016) 10288–10296.
- [48] M. Farouk, A. Abd El-Maboud, M. Ibrahim, A. Ratep, I. Kashif, *Spectrochim. Acta Part A* 149 (2015) 338–342.
- [49] L.F. Souza, P.L. Antonio, L.V.E. Caldas, D.N. Souza, *Nucl. Instrum. Methods Phys. Res. Sect. A* 784 (2015) 9–13.
- [50] L. Zhao, Z. Wang, D. Han, D. Tao, G. Guo, *Mater. Res. Bull.* 44 (2009) 984–988.
- [51] Z. Lin, P. Xiao, S. Sun, Y. Li, W. Song, P. Gao, L. Wang, H. Ning, J. Peng, *Appl. Phys. Lett.* 107 (2015) 112108.
- [52] L.-L. Min, L.-B. Zhong, Y.-M. Zheng, Q. Liu, Z.-H. Yuan, L.-M. Yang, *Sci. Rep.* 6 (2016) 32480.
- [53] Y.G. Ko, H.J. Lee, S.S. Shin, U.S. Choi, *Soft Matter* 8 (2012) 6273–6279.
- [54] I. Lauermann, A. Steigert, *J. Large-Scale Res. Facil. JLSRF* 2 (2016) 67.
- [55] A. Fischer, J. Jindra, H. Wendt, *J. Appl. Electrochem.* 28 (1998) 277–282.
- [56] M.K. Kayarkatte, Ö. Delikyan, C. Roth, *Chem. Electro. Chem.* 4 (2017) 404–411.
- [57] F. Gu, S.F. Wang, M.K. Lü, G.J. Zhou, D. Xu, D.R. Yuan, *J. Phys. Chem. B* 108 (2004) 8119–8123.
- [58] P.G. Rouxhet, A.M. Misselyn-Bauduin, F. Ahimou, M.J. Genet, Y. Adriaensen, T. Desille, P. Bodson, C. Deroanne, *Surf. Interface Anal.* 40 (2008) 718–724.
- [59] H. Maachou, M.J. Genet, D. Aliouche, C.C. Dupont-Gillain, P.G. Rouxhet, *Surf. Interface Anal.* 45 (2013) 1088–1097.
- [60] I.F. Amaral, P.L. Granja, M.A. Barbosa, *J. Biomater. Sci. Polym.* 16 (2005) 1575–1593.
- [61] D. Briggs, M. Seah, H. Bubert, *Angew. Chem.–German* 107 (1995) 1367.
- [62] B.D. Ratner, D.G. Castner, *In Surface Analysis: The Principal Techniques*, in: J.C. Vickerman (Ed.), Wiley, Chichester, England, 1997.
- [63] L. Wang, S. Dou, J. Xu, H.K. Liu, S. Wang, J. Ma, S.X. Dou, *Chem. Comm.* 51 (2015) 11791–11794.
- [64] W.-Y. Kao, W.-Q. Chen, Y.-H. Chiu, Y.-H. Ho, C.-H. Chen, *Sci. Rep.* 6 (2016) 37174.
- [65] W. Zhang, W. He, X. Jing, *J. Phys. Chem. B* 114 (2010) 10368–10373.
- [66] S. Rashid, C. Shen, X. Chen, S. Li, Y. Chen, Y. Wen, J. Liu, *RSC Adv.* 5 (2015) 90731–90741.
- [67] G. Panomsuwan, N. Saito, T. Ishizaki, *ACS Appl. Mater. Interfaces* 8 (2016) 6962–6971.
- [68] G. Liu, X. Li, J.-W. Lee, B.N. Popov, *Catal. Sci. Technol.* 1 (2011) 207–217.
- [69] J. Wu, L. Ma, R.M. Yadav, Y. Yang, X. Zhang, R. Vajtai, J. Lou, P.M. Ajayan, *ACS Appl. Mater. Interfaces* 7 (2015) 14763–14769.
- [70] F. Yang, H. Liu, J. Qu, J. Paul Chen, *Bioresour. Technol.* 102 (2011) 2821–2828.
- [71] S.-F. Lim, Y.-M. Zheng, S.-W. Zou, J.P. Chen, *Environ. Sci. Technol.* 42 (2008) 2551–2556.
- [72] Y. Zhao, R. Nakamura, K. Kamiya, S. Nakanishi, K. Hashimoto, *Nat. Comm.* 4 (2013) 2390.
- [73] J. Zhang, S.J. Deng, S.Y. Liu, J.M. Chen, B.Q. Han, Y. Wang, Y.D. Wang, *Mater. Technol.* 29 (2014) 262–268.
- [74] R. Yuvakkumar, S.I. Hong, *J. Sol-Gel Sci. Technol.* 73 (2015) 511–517.
- [75] T.-M. Pan, C.-W. Lin, J.-C. Lin, M.-H. Wu, *Electrochim. Solid State Lett.* 12 (2009) J96–J99.
- [76] A. Fetyan, I. Derr, M.K. Kayarkatte, J. Langner, D. Bernsmeier, R. Krahnert, C. Roth, *Chem. Electro. Chem.* 2 (2015) 2055–2060.
- [77] N. Wakabayashi, M. Takeichi, M. Itagaki, H. Uchida, M. Watanabe, *J. Electroanal. Chem.* 574 (2005) 339–346.
- [78] A. Damjanovic, D.B. Sepa, *Electrochim. Acta* 35 (1990) 1157–1162.
- [79] K.-H. Lee, S.B. Sinnott, *Nano Lett.* 5 (2005) 793–798.
- [80] X. Hu, Y. Wu, H. Li, Z. Zhang, *J. Phys. Chem. C* 114 (2010) 9603–9607.
- [81] G.A. El-Nagar, A.M. Mohammad, *Int. Hydrogen Energy* 39 (2014) 11955–11962.
- [82] A.M. Mohammad, G.A. El-Nagar, I.M. Al-Akraa, M.S. El-Deab, B.E. El-Anadolli, *Int. J. Hydrogen Energy* 40 (2015) 7808–7816.
- [83] G.A. El-Nagar, A.M. Mohammad, M.S. El-Deab, T. Ohsaka, B.E. El-Anadolli, *J. Power Sources* 265 (2014) 57–61.
- [84] G.A. El-Nagar, M.S. El-Deab, A.M. Mohammad, B.E. El-Anadolli, *Electrochim. Acta* 180 (2015) 268–279.
- [85] M.S. El-Deab, A.M. Mohammad, G.A. El-Nagar, B.E. El-Anadolli, *J. Phys. Chem. C* 118 (2014) 22457–22464.
- [86] M.S. El-Deab, F. Kitamura, T. Ohsaka, *J. Power Sources* 229 (2013) 65–71.
- [87] S.M. Unni, R. Illathvalappil, S.N. Bhange, H. Puthenpediakkal, S. Kurungot, *ACS Appl. Mater. Interfaces* 7 (2015) 24256–24264.
- [88] E. Proietti, F. Jaouen, M. Lefèvre, N. Larouche, J. Tian, J. Herranz, J.-P. Dodelet, *Nat. Comm.* 2 (2011) 416.
- [89] K. Strickland, E. Miner, Q. Jia, U. Tylus, N. Ramaswamy, W. Liang, M.-T. Sougrati, F. Jaouen, S. Mukerjee, *Nat. Comm.* 6 (2015) 7343.